The Impact of the Three-Dimensional Structure of a Subduction Zone on Time-dependent Crustal Deformation Measured by HR-GNSS

Oluwaseun Idowu Fadugba*[1], Valerie J. Sahakian[1], Diego Melgar[1], Arthur Rodgers[2] and Roey Shimony[1]

(1) Department of Earth Sciences, University of Oregon, Eugene, OR

(2) Lawrence Livermore National Laboratory, Livermore, CA

***Corresponding author: ofadugba@uoregon.edu**

This is a noon-peer reviewed pre-print submitted to EarthArXiv. This paper has been submitted to Seismica for review.

The Impact of the Three-Dimensional Structure of a Subduction Zone on Time-dependent Crustal Deformation Measured by HR-GNSS

Oluwaseun Idowu Fadugba[1], Valerie J. Sahakian[1], Diego Melgar[1], Arthur Rodgers[2] and Roey Shimony[1]

(3) Department of Earth Sciences, University of Oregon, Eugene, OR

(4) Lawrence Livermore National Laboratory, Livermore, CA

ABSTRACT

Accurately modeling time-dependent coseismic crustal deformation as observed on high-rate Global Navigation Satellite System (HR-GNSS) lends insight into earthquake source processes and improves local earthquake and tsunami early warning algorithms. Currently, time-dependent crustal deformation modeling relies most frequently on simplified 1D radially symmetric Earth models. However, for shallow subduction zone earthquakes, even low-frequency shaking is likely affected by the many strongly heterogeneous structures such as the subducting slab, mantle wedge, and the overlying crustal structure. We demonstrate that including 3D structure improves the estimation of key features of coseismic HR-GNSS time series, such as the peak ground displacement (PGD), the time to PGD (t_{PGD}), static displacements (SD), and waveform cross-correlation values. We computed 1D and 3D synthetic, 0.25 Hz and 0.5 Hz waveforms at HR-GNSS stations for four **M**7.3+ earthquakes in Japan using MudPy and SW4, respectively. From these synthetics, we computed intensity-measure residuals between the synthetic and observed GNSS waveforms. Comparing 1D and 3D residuals, we observed that the 3D simulations show better fits to the PGD and SD in the observed waveforms than the 1D simulations for both 0.25 Hz and 0.5 Hz simulations. We find

that the reduction in PGD residuals in the 3D simulations is a combined effect of both shallow and deep 3D structures; hence incorporating only the upper 30 km 3D structure will still improve the fit to the observed PGD values. Our results demonstrate that 3D simulations significantly improve models of GNSS waveform characteristics and will not only help understand the underlying processes, but also improve local tsunami warning.

INTRODUCTION

Real-time high-rate Global Navigation Satellite System (HR-GNSS) are key observational data for kinematic slip inversions (e.g., Ozawa et al., 2011; Melgar et al., 2016), an important lens into large earthquake rupture physics (e.g., Melgar and Bock, 2015), as well as for real-time applications in Earthquake and Tsunami Early Warning (EEW/TEW) (e.g., Sahakian et al., 2019b). Kinematic slip inversions, traditionally from broadband seismograms and strong motion data, are used for rapid and retrospective seismological studies to understand earthquake complexities through finite fault model, source time function and directivity etc. (e.g., Ide 2007, Goldberg et al., 2022). HR-GNSS waveforms are an important contribution to these models to constrain the time-dependent, low-frequency deformation of the Earth's surface. In the resulting finite fault model, this yields not only slip on the fault, but information about the rupture kinematics for each subfault, thus providing both spatial and temporal distribution of slip on a more granular level (e.g., Melgar and Bock, 2015; Melgar et al., 2020). When performed in real-time, rapid kinematic source models are an important component of TEW approaches (hence, better rapid local tsunami modeling). HR-GNSS data also provide crucial constraints for rapid earthquake magnitude estimation, in particular for large magnitude earthquakes as the displacement metrics they provide do not saturate, unlike displacement

obtained from those from broadband seismograms and strong motion data (e.g., Bock et al., 2011; Melgar et al., 2016; Sahakian et al., 2019b). In addition to constraining rapid finite-fault inversions for local TEW, the peak ground displacement (PGD) and time to reach peak ground displacement (t_{PGD}) as recorded by HR-GNSS can play a key role in discriminating tsunami earthquakes (TsEs) from non-TsEs (Sahakian et al., 2019b).

Static and kinematic slip inversion models using displacement time series from HR-GNSS waveforms are routinely performed using simplified 1D radially symmetric Earth models, by determining the displacement from each subfault with a 1D Green's function (Melgar and Bock, 2015), as it is oft assumed that three-dimensional heterogeneities play a smaller role in the low-frequency content of waveforms than for high-frequency seismic data. However, the availability of high-rate GNSS data and the need to resolve earthquake and wave propagation details with higher frequencies and shorter wavelengths exposes the inadequacy of 1D models for analysis of large earthquake ruptures. Many studies using 1D structure observed some delays and unmodeled features in the HR-GNSS waveforms from the 2011 moment magnitude (**M**) 9.0 Tohoku-Oki earthquake (Yue & Lay, 2011; Melgar & Bock, 2015), as well as other earthquakes (e.g., Delouis et al., 2010).

Subduction zones present unique three-dimensional challenges that may not be well-captured by 1D models. Due to complex geometry, the resultant onshore deformation and shaking from megathrust events is likely affected by many strongly heterogeneous structures such as the slab, the wedge, the overlying crustal structure, etc. However, current models of time-dependent crustal deformation, or low-frequency shaking, typically use Green's function approaches and 1D Earth structure, omitting the effects of the 3D Earth structure on the wave

path, hence on the observed waveforms. In this work, we present results comparing 1D to 3D models of time-dependent crustal deformation and find that three-dimensional effects are non-negligible, and should be an important component of kinematic modeling.

BACKGROUND

Previous studies have contributed to the advancement of slip models in a 3D Earth structure (e.g., Wald et al., 2001; Williams & Wallace, 2015, and Tung & Masterlark, 2018) and show that material contrasts between continental crust and oceanic slabs have a large effect on recovering static coseismic displacements, slow slip events, slip distributions and tsunami behavior in elastic models. For example, Tung and Masterlark (2018) show that the inclusion of heterogenous crustal structure can remove nonrealistic slip artifacts in slip distributions and reduce the misfit in large seafloor displacement that contributes to prediction error of tsunami amplitudes. William and Wallace (2015) also show a better fit to the observed GNSS displacements by computing Green's functions using a realistically varying elastic properties with a finite element method (Aagaard et al., 2013). Hearn & Burgmann (2005) shows similar effects in strike-slip settings, comparing 1D structure and homogenous half space models. They find an improvement in the estimation of the moment and centroid depth from GNSS measurements by incorporating earth's layered elastic structure in the slip inversion. This reduces the disparity between the geodetic and seismic moment estimates for large strike-slip earthquakes and suggests that time-dependent crustal deformation should be affected by depth-dependent elasticity. Langer et al. (2022) uses a synthetic model of sedimentary basin to investigate the impact of 3-D elastic structure on forward models of co-seismic surface

deformation and suggest the use of a layered velocity structure in static slip inversion in regions with sedimentary basins. Langer et al. (2019) show the importance of including topography in coseismic deformation modeling.

Together, these advances show that both static and dynamic (time-dependent) crustal deformation suffer from "path effects" in the same way that high-frequency time-dependent coseismic ground motions do. Path effects are a common source of uncertainty in ground motion models that focus on the effects of seismic waves' path on higher frequency intensity measures (Baltay et al., 2017; Sahakian et al., 2019a, Kotha et al., 2020; Landwehr et al., 2016; Kuehn & Abrahamson 2020; Zhang et al., 2022), and it stands to reason that they likely play a role in low to moderate frequencies (~1 Hz, that of HR-GNSS and time-dependent crustal deformation) as well.

Better modeling time-dependent, coseismic crustal deformation has significant contributions to improving our understanding of underlying large earthquake source processes, as well as improving warning and rapid response systems overall (Wirth & Sahakian et al., 2022). In this work, we show a comparison of 1D vs. 3D deterministic HR-GNSS waveforms for events in Japan to show the impact of 3D structure on accurately modeling GNSS waveforms. We choose Japan to test our hypotheses, as its seismicity, HR-GNSS recordings, and knowledge of 1D and 3D structures are ideal for our purposes. Japan has an excellent GNSS Network (~1178 stations), a good number of **M**7.3+ Earthquakes and Japan has both 1D and 3D velocity models (Fig. 1). We will show that the effects of including 3D structures is most important in improving the PGD at all hypocentral distances and SD residual values at stations generally and hypocentral distance above 350-400 km.

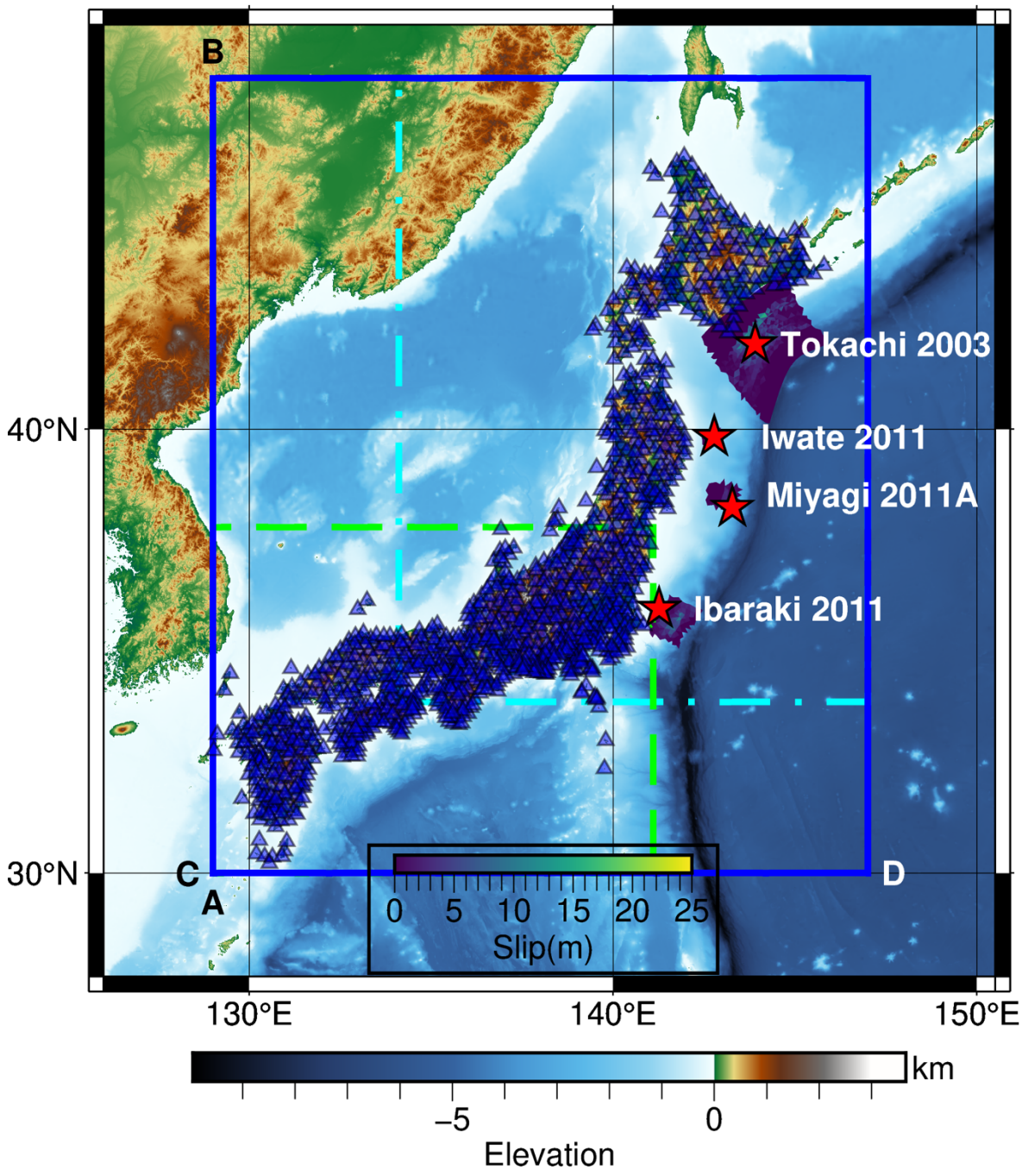

Fig. 1: Study region around Japan with topography and bathymetry showing the HR-GNSS stations (blue triangles) used to observe and model at least one earthquake (SNR³3). The figure also shows the four earthquake epicenters (red stars) used in this study and their published ruptures (colored by slip on the fault as described by below colorbar, see Table 1). The lines show the 3D Japan Integrated Velocity Structure Model (Koketsu et al., 2008, 2009) domains: West region (green dashed line), East region (cyan dashed-dotted line) and Combined full rfile (blue solid line). Edges AB and CD show the profile lines of the 3D Japan Integrated Velocity Structure Model presented in Fig. 4.

DATA AND METHODS

We generate 1D and 3D low-frequency synthetic GNSS waveforms of **M**7.3+ megathrust earthquakes in Japan and compare the 1D and 3D synthetics with the observed GNSS waveforms using several waveform intensity measures. We also test different rupture models for some of the earthquakes to investigate the effect of rupture model on the intensity measures.

Data

We focus on four **M**7.3+ megathrust earthquakes in Japan with good rupture models: 2011 **M**7.9 Ibaraki, 2011 **M**7.4 Iwate, 2011A **M**7.3 Miyagi and 2003 **M**8.3 Tokachi 2003 (Fig. 1; Table 1). We did not include the 2011 **M**9.0 Tohoku-Oki earthquake due to computational cost of the 3D simulations, but we expect similar conclusions with the **M**7.3+ earthquakes used in this study. We used the 1Hz GNSS waveforms from Ruhl et al. (2018), obtained using the Precise Point Processing approach and, from these, determine total horizontal displacement waveform (T(t)) using equation 1. We focused on the total horizontal displacement as the vertical displacement measurement in HR-GNSS are less accurate due to the distribution of GNSS satellites and generally assigned an error of about 3-5 times that of the horizontal (e.g., Geng et al., 2018; Melgar et al., 2020). The use of T(t) ensures that the more significant error in the vertical displacement compared to the horizontal displacement measurements is not influencing the 1D to 3D comparison, thus avoiding the misfit due to noise as opposed to the effect of the 3D structure.

$$T(t) = \sqrt{[N(t)^2 + E(t)^2]} \quad \text{..... (1)}$$

Table 1: Earthquakes used in this study and the corresponding rupture models. SN: Source Number.

SN	Event Name	Origin Time (UTC)	Latitude (°)	Longitude (°)	Depth (km)	Moment magnitude (**M**)	Number of GNSS Stations (SNR≥3)	Rupture Models and corresponding references
1	Ibaraki 2011	2011-03-11T06:15:34	36.1083	141.2653	43.2	7.9	737	SRCMOD (Kubo et al., 2013) Zheng (Zheng et al., 2020)
2	Iwate 2011	2011-03-11T06:08:53	39.8390	142.7815	31.7	7.4	271	Zheng (Zheng et al., 2020)
3	Miyagi 2011A	2011-03-09T02:45:12	38.3285	143.2798	8.3	7.3	240	Hayes (NEIC, 2014) Zheng (Zheng et al., 2020)
4	Tokachi 2003	2003-09-25T19:50:06	41.7750	143.9040	27.0	8.3	236	Hayes (NEIC,2014) SRCMOD (Koketsu et al., 2004) SRCMOD 2 (Yamanaka and Kikuchi, 2003) SRCMOD 3 (Yagi, 2004)

1D Simulation using FakeQuakes/MudPy

We used the FakeQuakes and MudPy software (Melgar et al., 2016) to generate 1D synthetic waveforms using a 1D velocity model in two steps. FakeQuakes first produces stochastic kinematic rupture models using published rupture model as mean slip model following the approach of Goldberg & Melgar, (2020). To do so, it uses a VonKarman correlation function to generate slip distributions from the perturbations around a known slip model given a target magnitude or mean slip distribution and a prescribed fault geometry. We then use MudPy to generate displacement time series from the kinematic rupture models with a Green's function approach using a 1D layered Earth. FakeQuakes/MudPy requires the fault and rupture models, 1D velocity model and the GNSS station locations as input parameters.

We used the Slab2.0 model (Hayes, 2018) to create a fault geometry mesh for the Japan Trench using Gmsh, a 3-D finite element mesh generator (Geuzaine and Remacle, 2009; Fig. S1). Details of the fault files are described in the supplementary material (S1). We focused on the Kuril region of Japan where the **M**7.3+ megathrust earthquakes used in this study are located. We use the published rupture models for the four megathrust earthquakes as input mean slip distributions for FakeQuakes (Table 1). For the Ibaraki 2011 earthquake, we used the Kubo et al. (2013) rupture model (henceforth referred to as SRCMOD) and Zheng et al. (2020; henceforth referred to as Zheng) rupture model. For the Miyagi 2011A earthquake, we used the NEIC (2014; henceforth referred to as Hayes) and Zheng rupture models. For the Tokachi 2003 earthquake, we used models from Koketsu et al. (2004), Yamanaka and Kikuchi (2003), Yagi (2004) (henceforth referred to as SRCMOD, SRCMOD2 and SRCMOD 3, respectively) and Hayes rupture models. We used only the Zheng rupture model for Iwate 2011 earthquake (Table 1).

The geometries of the published rupture models are planar and does not coincide with the geometry of Japan trench from Slab2.0, so, we project the slip in the rupture model for each earthquake onto the fault geometry (Fig. S2, https://doi.org/10.5281/zenodo.7765170). With FakeQuakes, we generated 100 realizations of the published rupture models using the published model as a mean model. In Figure 2 show mean rupture model (SRCMOD) for Ibaraki 2011 earthquake (Kubo et al., 2013) and three examples of the 100 FakeQuakes ruptures realizations from the mean rupture model. The mean rupture models and examples of FakeQuakes ruptures of the other earthquakes used in this study are in the Supplementary material (Fig. S3-S4).

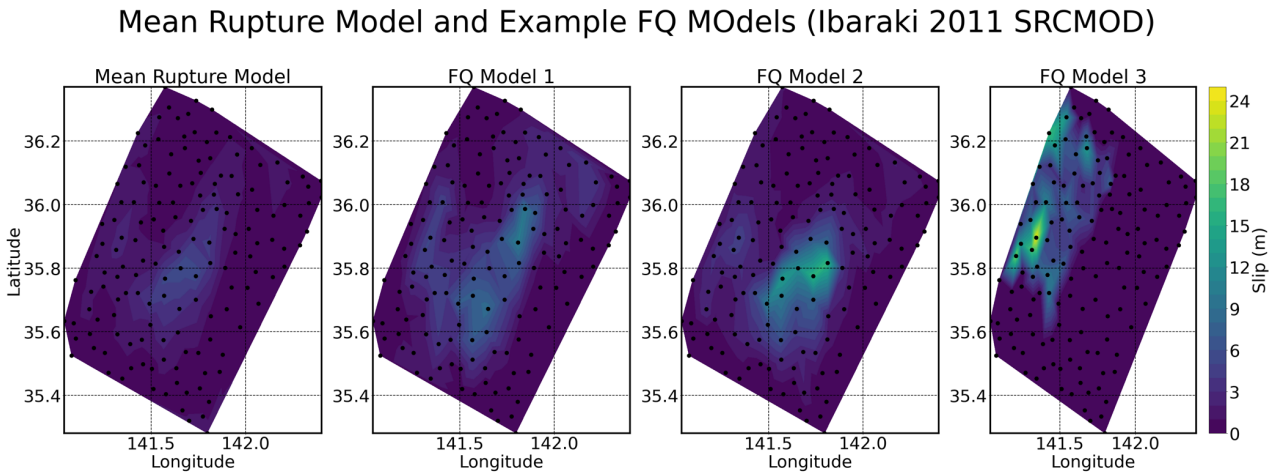

Fig. 2: Mean Rupture model (SRCMOD) for Ibaraki 2011 earthquake (Kubo et al., 2013) and three examples of the 100 FakeQuakes (FQ) ruptures realizations from the mean rupture model. The color indicates the amount of slip per subfault, and the black dots signify the center of each subfault. The slip is greater overall in the FakeQuake models compared to the mean slip model in the top left to conserve the moment release in response to the change in rigidity at the subfault locations compared to the one used to generate the mean slip model. FQ Model 3 is an end-member example of a rupture model with different slip pattern compared with the mean slip model, but with similar moment release.

We adopted the 6-layer crustal velocity structure of Hayes (2017) for all the earthquakes for its simplicity and the ease to set it up in our 1D and 3D simulations (Fig. 3). We used the isotropic Preliminary Reference Earth Model (PREM) from 40 to 200 km depth (Dziewonski and Anderson, 1981). There are other well-known 1D velocity models for Japan that could be used (e.g., VJMA, 2001; Hayes, 2014; Laske et al., 2013). The Japan Meteorological Agency (JMA) uses a 1D velocity model (VJMA, 2001) to locate earthquakes in Japan. However, the model has a series of 500 m thick layers which are less practical to setup for our 3D simulations, and we aim for consistency in the 1D structure between 1D and 3D simulations.

The earthquakes were recorded on a total of 1178 GNSS stations, however, to reduce computation time, we only simulate waveforms for stations with an observed total horizontal

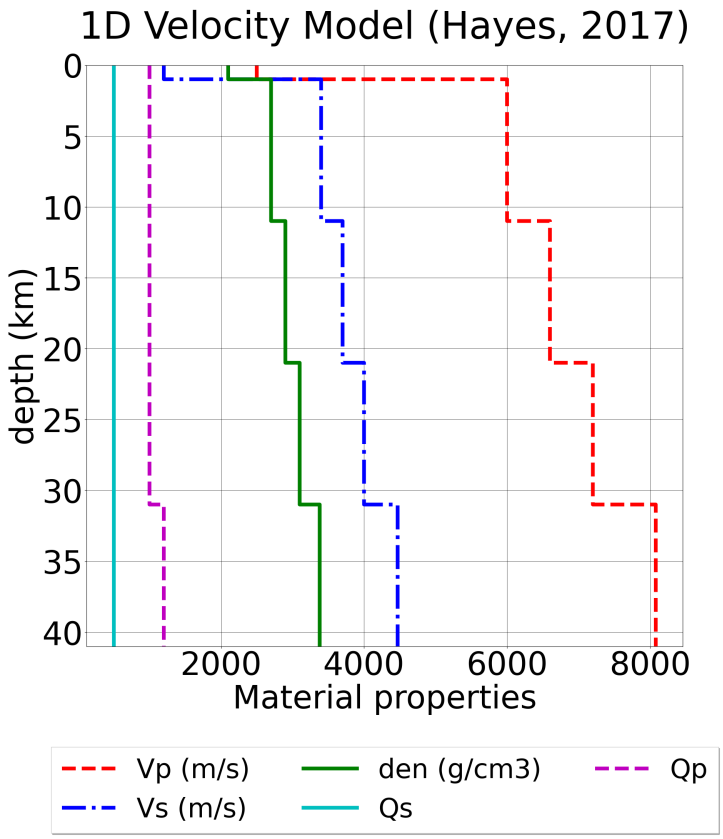

Fig. 3: 1D velocity model of Japan (Hayes, 2017) showing the P-wave velocity profile (red dashed line), S-wave velocity profile (blue dashed line), density profile (green solid line), and P- and S-wave quality factors (Qp and Qs) profiles (purple dashed line and cyan solid line, respectively). We used this 1D velocity model for the upper 40 km and the PREM model (Dziewonski and Anderson, 1981) from 40 km up to 200 km.

displacement signal-to-noise ratio (SNR, equation 2) larger than or equal to 3, thus reducing the number of stations for each earthquake simulation (Table 1).

$$\text{SNR} = \frac{\sigma_{\text{signal}}}{\sigma_{\text{noise}}} \quad \text{.....(2)}$$

where σ_{signal} is the standard deviation of 120s of recorded ground shaking after the P-wave arrival time while σ_{noise} is the standard deviation of 10s recordings before the P-wave arrival time. P-wave arrival time is defined as the origin time plus an approximate P-wave travel time (i.e., hypocentral distance between HR-GNSS station and rupture model hypocenter, divided by 6.5 km/s).

To understand the impact of the source rupture model on our synthetic waveforms, we investigated the effect of rupture models in the 1D simulations using two rupture models for the 2011 **M**7.9 Ibaraki and 2011A **M**7.3 Miyagi earthquakes and three rupture models for 2003 **M**8.3 Tokachi earthquake and compare their residuals.

SW4 3D Simulations

Our 3D synthetic waveforms were computed using SW4 2.01 (Sjögreen and Petersson, 2012; Petersson and Sjögreen, 2012; Petersson and Sjögreen, 2017a; Petersson and Sjögreen, 2015; Petersson and Sjögreen, 2017b) published under the GPL 2 license. SW4 solves the seismic wave equations in displacement formulation using a 4^{th} order accurate summation-by-parts finite difference method, a 3D model of velocity structure, and a domain geometry that includes both topography and bathymetry. Because this process is so computationally intensive, similar to the large-scale SW4 simulations of earthquakes on the Hayward Fault (Rodgers et al., 2020), we generated simulations for all four events at both 0.25 and 0.5 Hz, to compare with observations and understand if characteristic intensity measures such as PGD require information from higher frequencies.

We used the 3D Japan Integrated Velocity Structure Model (Koketsu et al., 2008, 2009) which includes topography and bathymetry dataset from the ETOPO1 1 arc-minute global relief model (NOAA National Geophysical Data Center, 2009) spanning a lateral extent of latitude from 30° to 47° North (~2040 km) and longitude from 129° to 147° (~1440 km) East. We convert the original ifile format of the 3D velocity structure to an rfile (Fig. 4). An rfile is a binary structured grid format, and it is the most efficient and realistic method to input 3D velocity

structure to SW4, as it is more effective for smoothly varying 3D heterogenous structure (Petersson and Sjögreen, 2017), hence more suitable for this study. The 3D Japan Integrated Velocity Structure Model (JIVSM) comprises 23 layers, each with constant P- and S-wave velocities (Vp and Vs), density (r) and P- and S-wave quality factors (Qp and Qs) (Table S1). The 3D structure is given in two overlapping sections (East and West Japan, Fig. 1), but were combined to create the unified 3D velocity model of Japan by extrapolating the top of each layer to regions outside the 3D structure regions following the OpenSWPC methodology (Maeda et al., 2017). The resulting rfile has 5 blocks with increasing grid spacing with depth: grid spacing of 200 m at the top to 1000 m at the bottom of the rfile. Details of the rfile are in the Supplementary material (S2).

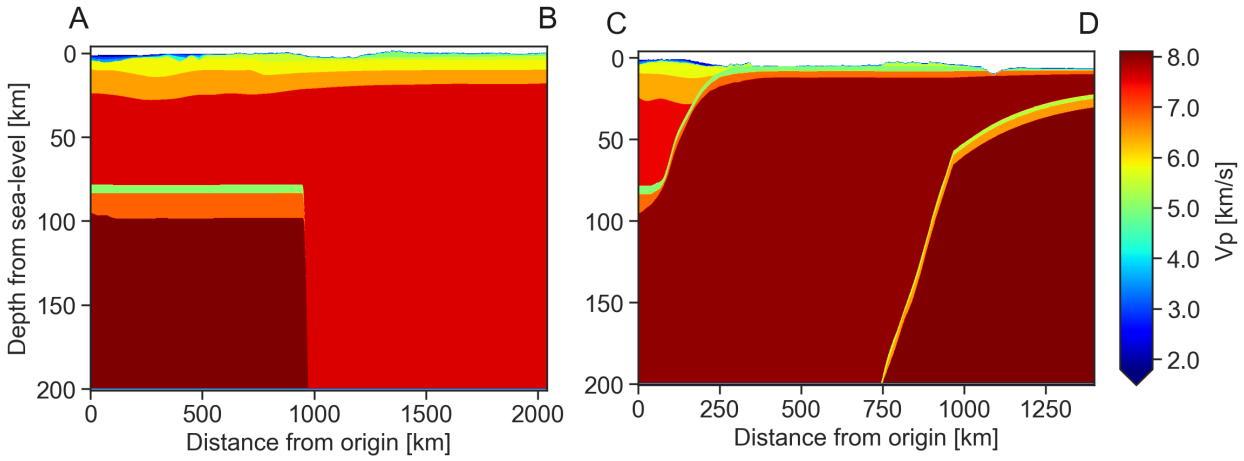

Fig. 4: 3D Japan Integrated Velocity Structure Model (JIVSM, Koketsu et al., 2008, 2009) showing AB and CD profile lines on a topography/bathymetry map in Figure 1. The profile AB show the geometries of the two subducting slabs and profile line CD best shows the heterogenous velocity structure in the upper 30 km depth of the 3D velocity structure.

Our domain depths extended from the surface (topography and bathymetry) to a maximum depth of 200 km. The maximum achievable frequency (f_{max}) is dependent on the grid size of the domain, as well as the minimum shear wave speed, as described by:

$$f_{max} = \frac{minV_s}{PPW \times h} \quad \text{..... (3)}$$

We used 8 Points Per Wavelength (PPW) in the simulations and the minimum shear wave speed ($minV_s$) value of 1200 m/s based on the average V_S value in the upper 400 m in the 3D velocity model (equation 3; Petersson and Sjögreen, 2017b). To generate 3D synthetic waveforms with a maximum frequency of 0.25 and 0.5 Hz, we used a minimum grid spacing (h) of 600 and 300 m, respectively. We use a curvilinear mesh from the surface (topography and bathymetry) to 30-km depth with a grid spacing of 300 m and used Cartesian mesh from 30 km downwards. Within the Cartesian mesh, we applied grid refinement at 75 km depth to reduce the computational resources required for these simulations. Our vertical grid spacing increased with depth and the associated increasing $minV_s$: 300 m and 600m grid spacing for the 30-75 km and 75 – 200 km depth range, respectively. For the 0.50 Hz SW4 simulations, we varied the lateral extent of the 3D domain geometry depending on location of each earthquakes (Fig. S5) to limit the maximum memory required by the simulations to ~4TB (Supplementary material S3). We compared only the intensity measures from the common stations between the 1D and 3D simulations.

For the 0.25 Hz simulations, we selected two of the 100 rupture models from FakeQuakes for each earthquake and read them into SW4 format using the Standard Rupture Format (SRF) version 2.0 source representations (Graves, 2014). We used only one rupture model for the 0.5 Hz simulations due to their high computational cost.

Comparing 1D vs. 3D Synthetic Waveforms

We compare the 1D and 3D synthetics with the observed GNSS waveforms using the total horizontal component waveforms. In addition to wiggle-to-wiggle comparisons via waveform cross-correlation (xcorr) with time-shifting for both 1D and 3D synthetics, we also model the average behavior of important features of the observed waveforms over many realizations from the mean rupture models. We measure the goodness of fit by comparing the misfits of the total horizontal waveform synthetic and observed waveforms using waveform intensity measures such as the Peak Ground Displacement (PGD), the time it takes to reach the PGD (t_{PGD}), static displacement residuals (SD), each described in Figure 5.

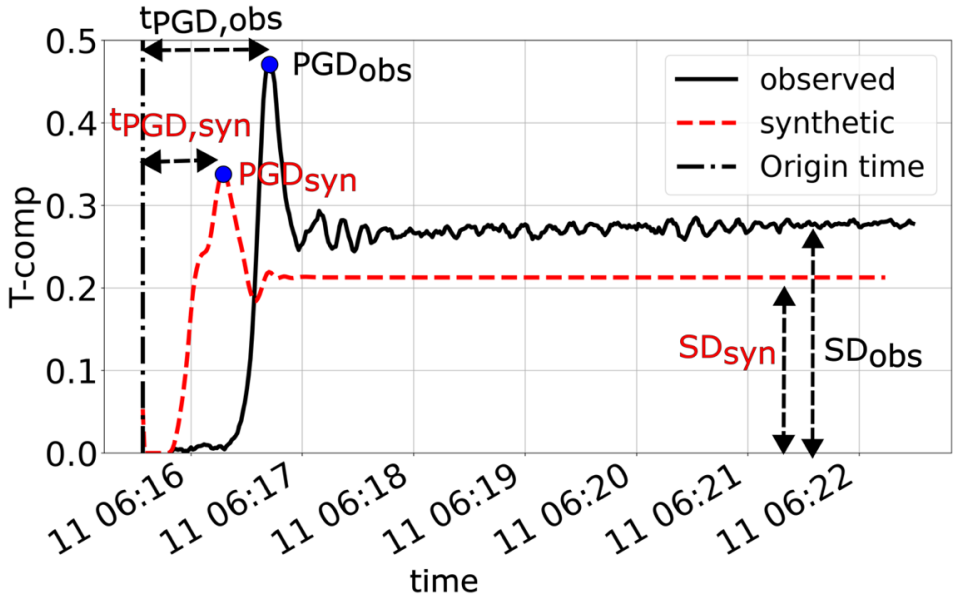

Fig. 5: Schematic representation of the definitions of the intensity measure definitions used in comparing the total horizontal waveform synthetic ("syn") and observed ("obs") waveforms. Black solid and red dashed lines are the observed and synthetic waveforms, respectively. The blue dots show the Peak Ground Displacement (PGD) for the observed and synthetic waveforms and their corresponding time to reach the PGD (t_{PGD}). The figure also shows the definition of static displacement (SD). The amplitude and time axes values in this figure are arbitrary.

We then determine the residuals for the PGD and SD intensity measures (equation 4a). A residual (δ_{ij}) of 0 corresponds to perfect equivalence between observed (obs) and synthetic (syn) values, while residual values of 0.5 and 1.0 signify that the observed value is 1.6x and 2.7x the synthetic values, respectively. For the t_{PGD} residuals, we use the time difference between the time it takes to reach the PGD for observed and synthetic waveforms (equation 4b). Cross-correlation values inherently compare the fit between observed and synthetic waveforms.

$$\delta_{ij,PGD} = \ln\left(\frac{PGD_{obs}}{PGD_{syn}}\right) \quad \text{(4a)}$$

$$\delta_{ij,t_{PGD}} = t_{PGD,obs} - t_{PGD,syn} \quad \text{(4b)}$$

We investigate the variation of each intensity measure with distance by binning the intensity measures with respect to the hypocentral distance (R_{hyp}), the distance between rupture model hypocenter and the HR-GNSS station. The residuals in each bin are plotted using box and whisker plots. These combine the minimum and maximum values with the quartiles into one useful graph. It consists of a horizontal line, drawn according to scale, from the minimum to the maximum data value, and a box drawn from the lower to upper quartile with a vertical line marking the median. We removed the outliers outside the whiskers to improve readability.

RESULTS AND DISCUSSIONS

Comparing 1D and 3D residuals

First, as a control, we study the impacts of varying only the source model by investigating the residuals using only 1D velocity structure, with different published rupture models. The PGD residuals ($\delta_{ij,PGD}$, equation 2a) for all the earthquakes in the 1D simulations increase with

distance but are generally below 2 (Fig. 6). On each boxplot, residuals for each model are shown as patterned box and whisker plots, including blue circle patterns (SRCMOD), orange grid (SRMOD 2), light blue circled (SRCMOD 3), gray slanted (Hayes), and orange diamonds (Zheng). The red horizontal line represents the zero residual line. In the 1D simulations, PGD residuals do not change significantly with distance when we used different rupture models for the same earthquake (e.g., Hayes, SRCMOD, SRCMOD2, and SRCMOD3 for the 2003 Tokachi earthquake). Therefore, any deviations in the PGD residual for the same rupture model in 3D simulations are most likely due to the 3D Earth structure.

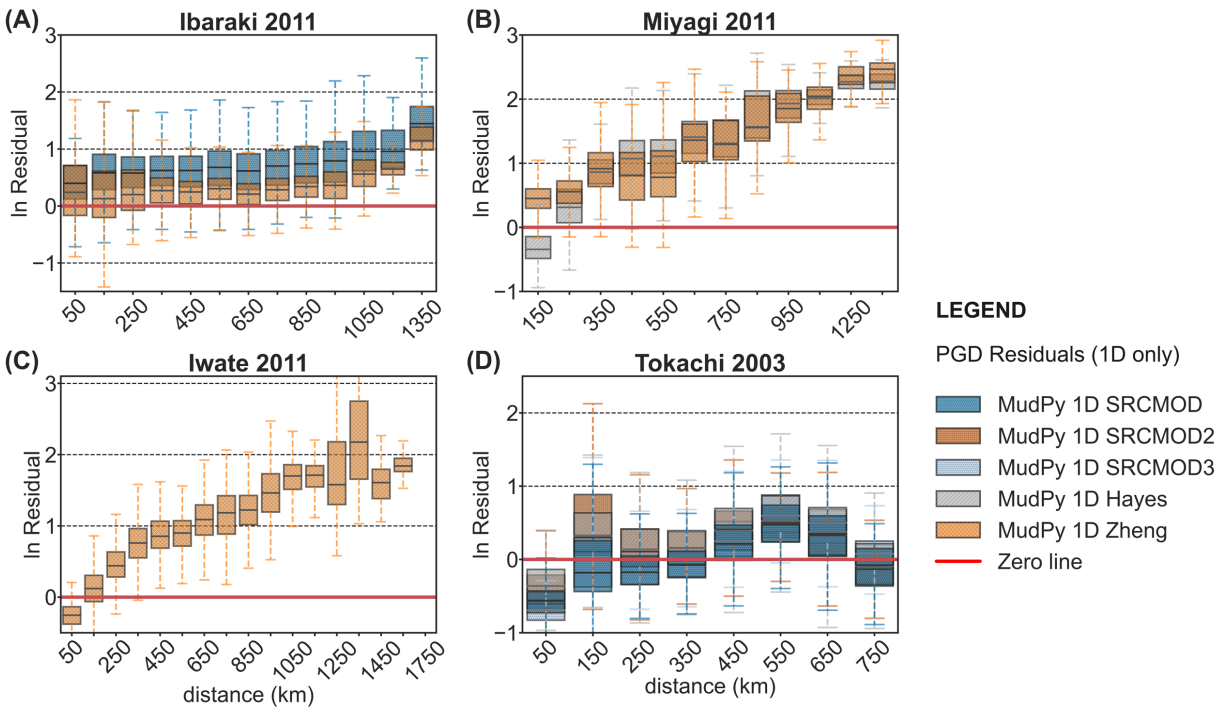

Fig. 6: PGD Residuals using only the 1D velocity model, demonstrating the effects of varying solely the source model for all the four earthquakes using for all the 100 random realizations of the mean rupture model. (A, B and D) shows the effect of rupture models on the PGD residuals from 1D simulations using Ibaraki 2011, Miyagi 2011A and Tokachi 2003 earthquakes. On each boxplot, residuals for each model are shown as patterned box and whisker plots, including blue circle patterns (SRCMOD), orange grid (SRMOD 2), light blue circled (SRCMOD 3), gray slanted (Hayes), and orange diamonds (Zheng). The red horizontal line represents the zero residual line.

The effect of this is exemplified in the comparison of the observed and the MudPy 1D and SW4 0.25 Hz and 0.5 Hz synthetic waveforms at stations 0041 and 0043 for the Ibaraki 2011 earthquakes for one of the 100 FakeQuake ruptures using the SRCMOD mean rupture model (Kubo et al., 2013) (Fig. 7). The MudPy 1D waveforms are very simple, but the SW4 waveforms better capture the variability in the observed waveforms. Specifically, the 3D waveforms and in particular the higher frequency 3D waveforms better capture the dynamic shaking in addition to the static offset observed at each station. This includes capturing a commonly observed dynamic overshoot, such as that observed in the North component of stations 0041 and 0043 for the Ibaraki earthquake, at ~60s (Fig. 7).

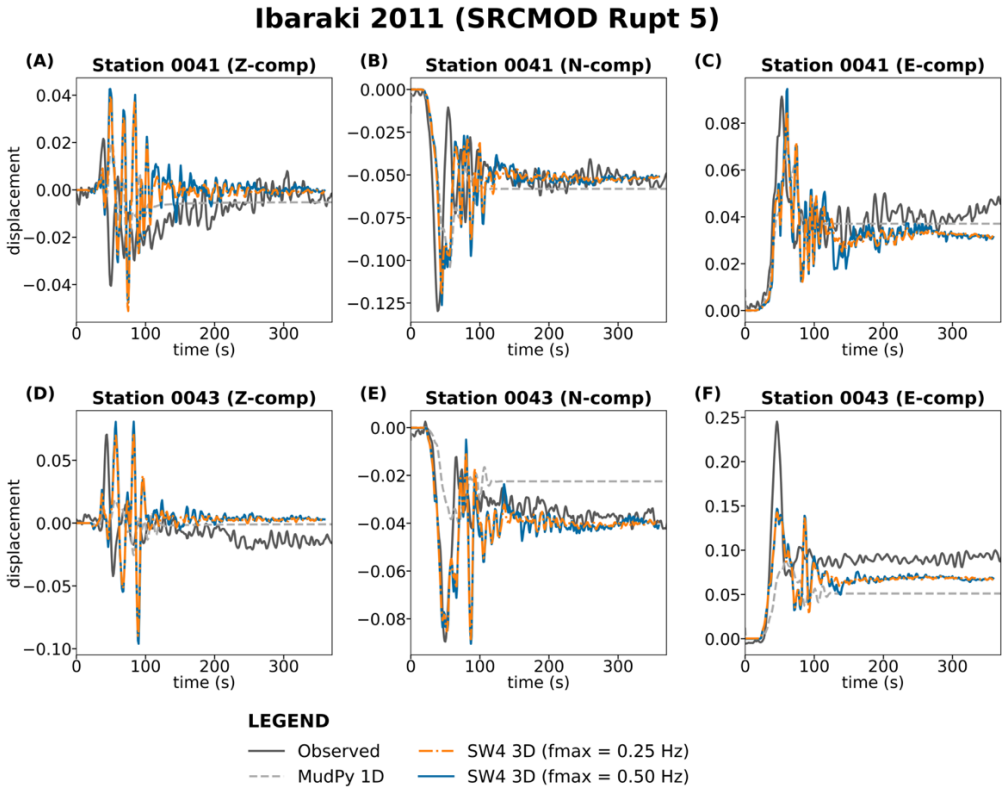

Fig. 7: Comparing the observed (dark gray solid line) and three synthetic waveforms: MudPy 1D (dashed gray line), SW4 0.25 Hz (dashed-dotted orange line) and 0.50 HZ (blue solid line) waveforms at stations 0041 and 0043, respectively. The MudPy 1D waveforms are very simple, but the SW4 waveforms better capture the variability in the observed waveforms. The observed waveforms were shifted back by 20 s to fit the synthetic waveforms. The figure shows the vertical (Z-comp) and the horizontal components (N-comp and E-comp) of the waveforms.

In a map view, we further show the effect of the 3D structure by overlaying the magnitude of velocity waveforms at the surface as a function of time on a topography/bathymetry map to highlight the spatial and temporal variation of the wavefront as it propagates (Fig. 8). The wavefronts appear spherical up to about 120s (Fig. 8E) and reveal a strong energy propagating SE away from the land. At 140s (Fig. 8F), the wavefronts show evidence of a waveguide on the shallow slab as the energy propagates at a lower velocity within the wedge area exemplifying the effect of the 3D structure. The extent of the packet of energy coincides with the geometry of the Japan trench. The packet of energy within the wedge continues to propagate northward and wavefront propagates through Japan. At 200s (Fig. 8H), the wavefronts reveal a basin effect in the Nankai and Sagami Troughs located SW of the Japan Trench and the in the Sea of Japan. The wavefront also shows a waveguide phenomenon in the shallow slab of the Nankai Trough and the packet of energy propagates westward with at slower velocity in the wedge even though the earthquake is located on the Japan Trench. From 270s onwards (Fig. 8J), the wavefront traveling northward through the wedge appears to bifurcate into the bay region towards Tomakomai and the other energy continues northward within the wedge. The observed waveguiding in the shallow slabs and the wave amplification in the Nankai and Sagami Troughs area show that lower frequencies still demonstrate non-negligible path effects, which may be important to the seismic hazard of Japan. Furthermore, this demonstrates that three-dimensional effects are important to include in kinematic slip models, as they may currently be wrapped into the source model.

This observation is distinctly different from the subduction guided waves observed from deep earthquakes on the subducting Pacific plate in Japan (Furumura and Kennett, 2005), as well as other regions globally (Furumura & Kennett, 1998; Furumura & Singh, 2002; Sahakian et al., 2018; Mann & Abers, 2020). In Japan, Furumura & Kennett (2005) observed an anomalously large intensity on the eastern seaboard of northern Japan from deep-seated earthquakes and the waveforms show a low-frequency ($f< 0.25$ Hz) onset for both P and S waves, followed by large, high frequency ($f>2$Hz) later arrivals with a long coda. They did not observe the

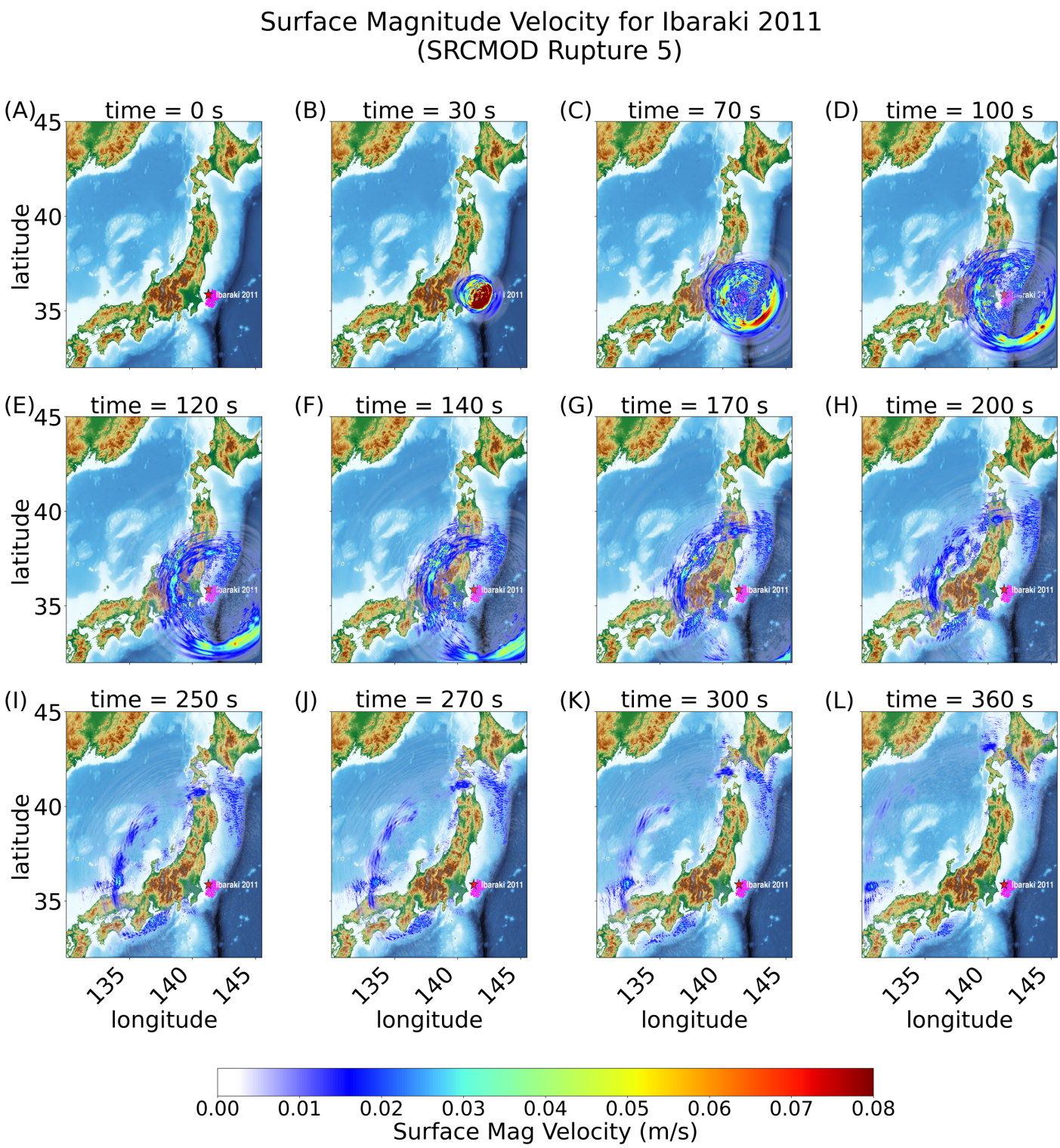

Fig. 8: Waveform propagation of Ibaraki 2011 earthquake using rupture 5 of the 100 FakeQuakes random realizations of the SRCMOD mean rupture model (Kubo et al., 2013), showing the effect of 3D velocity structure. The maximum frequency of the simulation is 0.25 Hz. The rupturing subfaults are shown as pink grid cells, and hypocenter as a star. Colorbar shows the surface magnitude velocity in m/s.

characteristics of frequency-selective wave propagation for subduction zone earthquakes with hypocenter depth less than 185 km. They explained this observation to arise from scattering of seismic waves by an elongated scatterer parallel to the plate margin. Despite the similarity in the phenomenon, the hypocenter of Ibaraki 2011 earthquake shown in Figure 8 has a hypocenter depth of 43.2 km and the maximum frequency in the waveforms are 0.25 Hz. We observed that the intense shaking is concentrated within the shelf regions and is bounded by the trench geometry. This shows that the shaking may be due to waveguide phenomenon is in the shallow slab within the low-velocity wedge. Indeed, in other subduction zones such as the Hikurangi, the sedimentary wedge is demonstrated to act as a waveguide, increasing shaking and dynamic stresses for longer period ground motions (Wallace et al., 2017; Kaneko et al., 2019). A more detailed examination of the waveguide is beyond the scope of this paper.

The PGD, t_{PGD}, SD residuals and cross correlation residual maps for the Ibaraki 2011 earthquake showing the spatial variation of the residuals are in the supplementary materials (Fig. S7). The PGD residual is generally near zero and positive, but < ln 1. We observed the residual is more positive near the coastal region of the Nankai Trough. However, an isolated zone with negative PGD residuals is observed near Kanazawa at the Japan Sea Margin. The t_{PGD} is generally positive and below 50 s, but slightly negative on the Japan Sea Margin. It is also noteworthy that the static displacement residuals are generally near zero but becomes more variable farther away from the hypocenter, especially toward SW Japan. The cross-correlation values between the SW4 3D waveforms and the observed waveforms shows a decay in values with distance but generally above 0.7.

Residual Analyses

Comparing 1D and 3D residuals, we observed that the 3D simulations residuals are clearly near zero (closer to the observed intensity measures) than the 1D residuals at all distances, except for the Tokachi earthquake (Fig. 9 and S8). The distributions of the intensity measures show improved fitting to the observed waveforms

in the 3D simulations. These results suggest that accounting for path-specific 3D structure improves the fit to the observed waveforms compared to the 1D simulations.

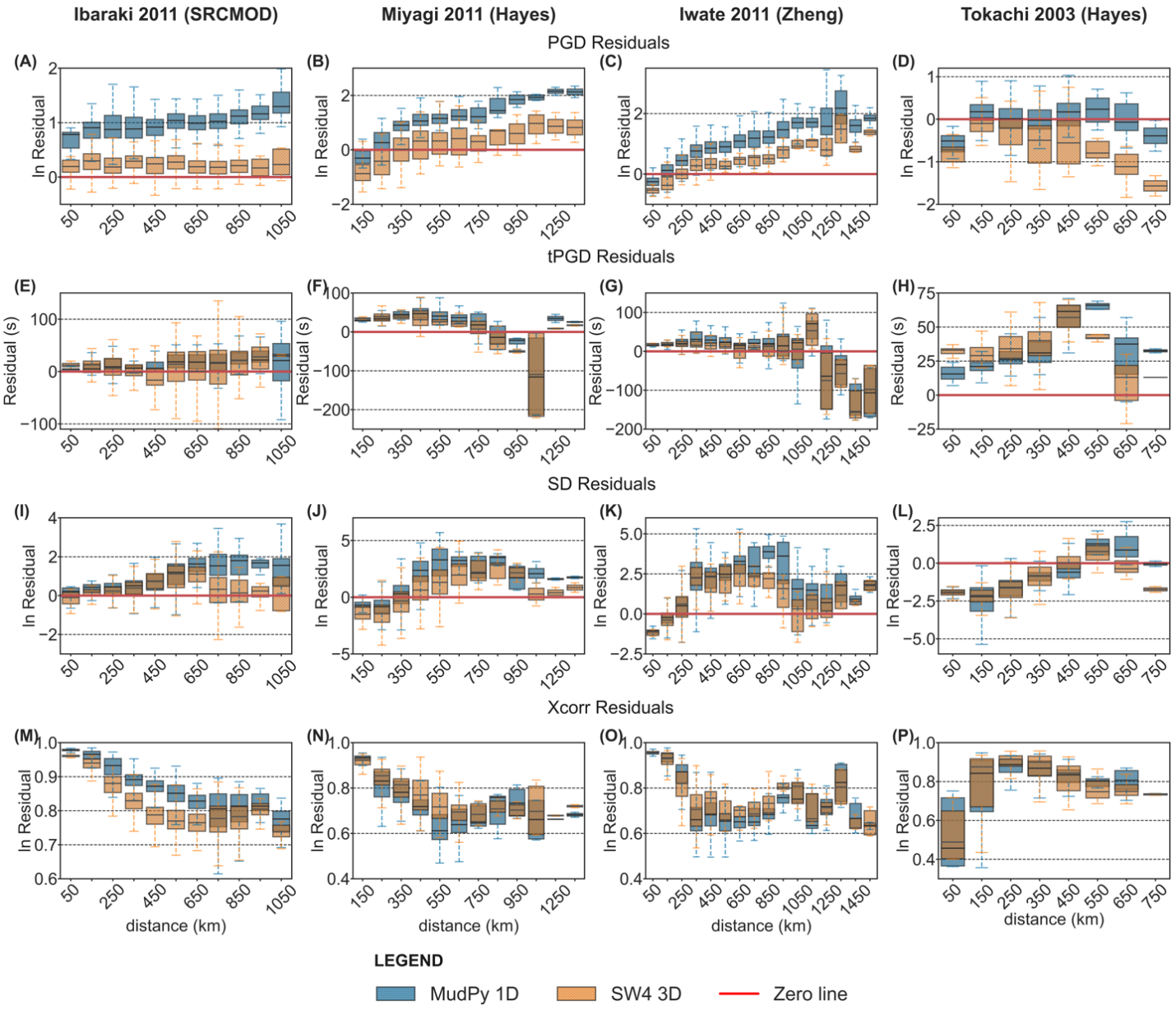

Fig. 9: Comparing MudPy 1D vs SW4 3D residuals between the synthetic to observed GNSS waveforms for Ibaraki 2011 (SRCMOD), Miyagi 2011 (Hayes), Iwate 2011 (Zheng) and Tokachi 2003 (Hayes rupture model) with f_{max} = 0.25 Hz. Figure (A-D) PGD residuals, (E-H) t_{PGD} (s) residuals, (I-L) static displacement residuals and (M-P) cross correlation values. We compare only the residuals of two corresponding rupture models in the MudPy and SW4 synthetic simulations. The blue boxplots with circle hatched filling represents the MudPy 1D residuals while the orange boxplot (diamond hatch style) represents the SW4 3D simulation. The red horizontal line represents the zero residual line.

For a more quantitative aggregate comparison, we determine the difference between the magnitude of the 3D median residuals compared to 1D median residuals for each residual boxplot (equation 5, Fig. 10). We compute the difference as:

$$\delta_{|3D|-|1D|} = |\delta_{3D}| - |\delta_{1D}| \quad \text{..... (5)}$$

where $|\delta_{1D}|$ and $|\delta_{3D}|$ are absolute values of the 1D and 3D median residuals, respectively. The median residual difference measures how much 3D median residual is closer to the zero value (i.e., fits the observed waveform) than the 1D simulations. A negative value of median residual difference shows that 3D simulations fit better to the observed intensity measure than the 1D simulations and vice versa. Note that this convention is different for the median residual difference for the cross-correlation values because a positive median residual difference for the cross-correlation shows that the 3D simulations fit the observed waveforms better.

To determine if the 1D and 3D residuals are statistically different from each other (i.e., come from different distributions), we perform Komogorov-Smirnov (K-S) tests (Kolmogorov, 1933; Smirnov, 1948) on the 1D and 3D residuals for each earthquake. Two distributions are significantly different when the statistical value (KS-stat) is above a critical value (D_{crit}) which is a function of the number of samples of each distribution and when the p-value is below the significance level of 0.05.

Considering the variation of the median residual of the intensity measures with distance, 3D simulations consistently have lower PGD median residuals (Fig. 10A) for all simulations with statistical significance (Fig. 10B), except for Tokachi 2003 (Fig. 10A). The t_{PGD} median residuals are consistently lower in the 3D simulations, generally between 250 and 700 km hypocentral distance except for the Ibaraki 2011 earthquake (Fig. 10C). The static-displacement median residuals are similar up to about 400 or 500 km (i.e., near zero), but the 3D simulations fit the observed static displacement better at longer distances (i.e., negative) (Fig. 10E). The cross-correlation median values are slightly higher in the 3D simulations, especially above distances of about 300 km, except for the Ibaraki 2011 earthquake (Fig. 10G).

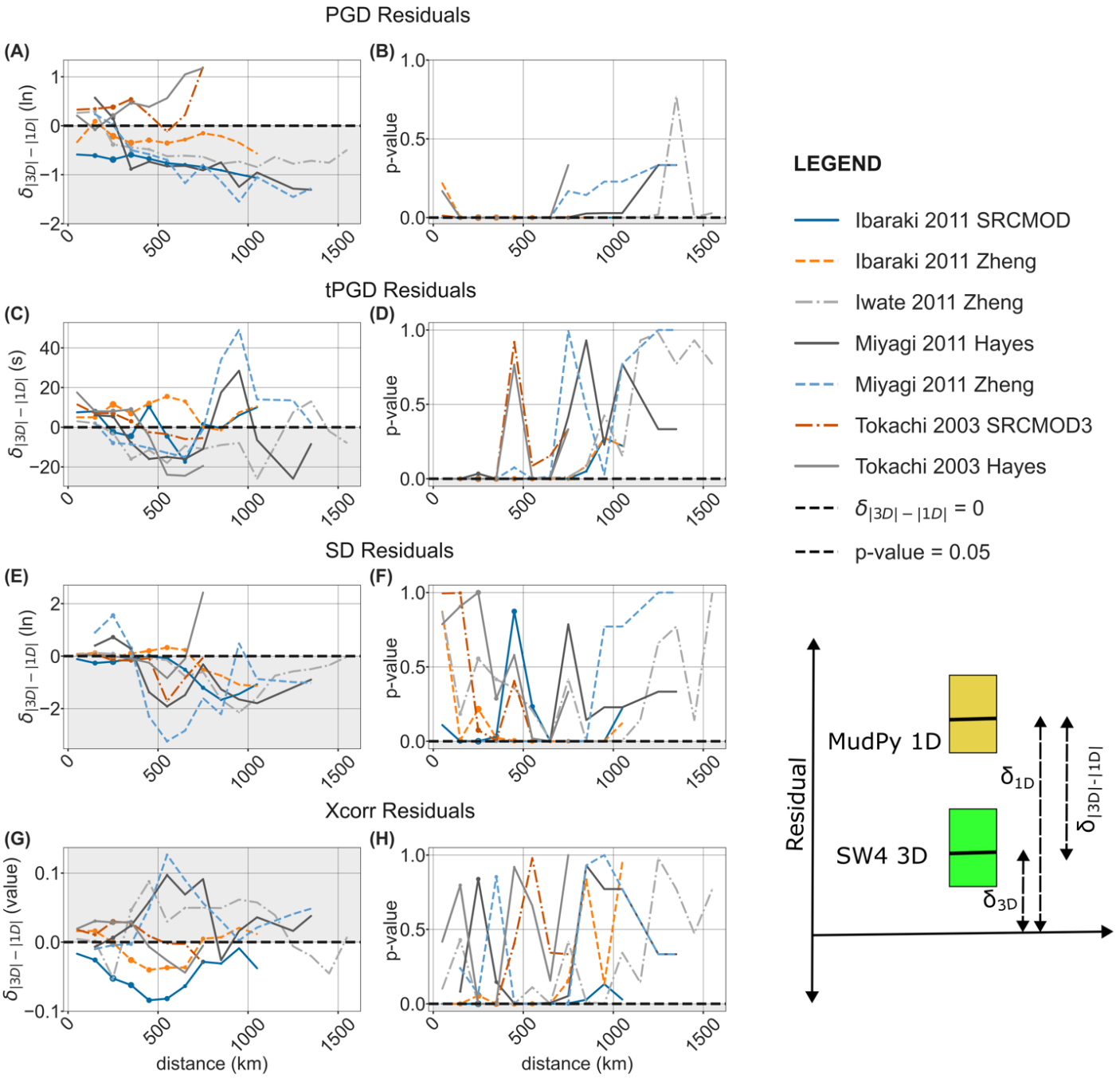

Fig. 10: Median residual difference and the P-value for the PGD, t_{PGD}, SD residuals and cross correlation values for all the simulations. Blue solid lines: Ibaraki 2011 SRCMOD, orange dashed lines: Ibaraki 2011 Zheng, gray dashed-dotted line: Iwate 2011 Zheng, Black solid lines: Miyagi 2011 Hayes, blue dashed lines: Miyagi 2011 Zheng, orange dashed-dotted lines: Tokachi 2003 SRCMO3, gray solid lines: Tokachi 2003 Hayes simulations. The gray shaded regions in (A), (C), (E) and (G) represents regions where "3D fits better than 1D" while the white regions represent "1D fits better than 3D". The gray shaded region in (B), (D), (F) and (H) represents regions where 1D and 3D residuals are statistically different from each other (i.e., come from different distributions) while the white regions represent 1D and 3D are from the same distribution. The bottom right schematic is a visual representation of the meaning of the mean residual difference.

The plots of the p-value with distance for all the earthquakes show that the comparison between 1D vs 3D intensity measure residuals vary with distance for all simulations (Fig. 10). Specifically, the KS tests show that the distributions of the PGD residuals in the 1D and 3D simulations are significantly different for all simulations up to hypocentral distance of 1000 km, and below 700 km for the Miyagi 2011 simulations (Fig. 10B). The t_{PGD} residual distributions are significantly different below 600 km distance, except for Ibaraki 2011 earthquake below 400 km, which corresponds to the distance range there is a better fit in PGD residuals for the 3D simulation (Fig. 10D). For both PGD and t_{PGD} residuals, the numbers of samples are generally smaller where the distributions are not significantly different. Conversely, the p-value plots for the static displacement and cross correlation show similar distributions between the 1D and 3D residuals (Fig. 10F and H).

The observed consistent overall increase in 1D and 3D residuals with distance may be because the source rupture model was derived with a 1D Green's function. The general trends in the PGD residuals show the 1D and 3D synthetic amplitudes generally decay faster than the observed amplitudes with distance, suggesting the variation in attenuation values within a layer unit in the 3D earth structure. Evaluation of the effect of the 1D velocity-derived rupture model and possible variation of attenuation within a layer on the general trend is beyond the scope of this study.

General Intensity Measure Residuals for each earthquake

The intensity measures for each simulation without considering the variation with distance show that the 1D vs. 3D residual distributions are significantly different for all simulations and there is a general reduction in the median residual values (hence, a better fit) in the 3D simulations compared to 1D simulations (Fig. 11).

Of greatest significance, we observed that the PGD residuals in the 3D simulations are smaller by about 0.4 -0.6 units compared to 1D simulations for all simulations, except for Tokachi 2003 (Hayes and SRCMOD3) models. Also, the t_{PGD} in the 3D simulations, in general, better fit the observed than 1D simulations by about 4

seconds, except for Ibaraki Zheng and Tokachi earthquake simulations. There is a slight reduction in the median static displacement residuals in the 3D simulations except for Ibaraki 2011 (Zheng) and Miyagi 2011 (Hayes) simulations. The 3D simulations generally have higher median cross-correlation values than 1D simulations, up to about 0.03. These results demonstrate that 3D structure plays a large, and statistically significant, role in accurately modeling the PGD and SD, as well as time-dependent characteristics of displacement time series (Fig. 11).

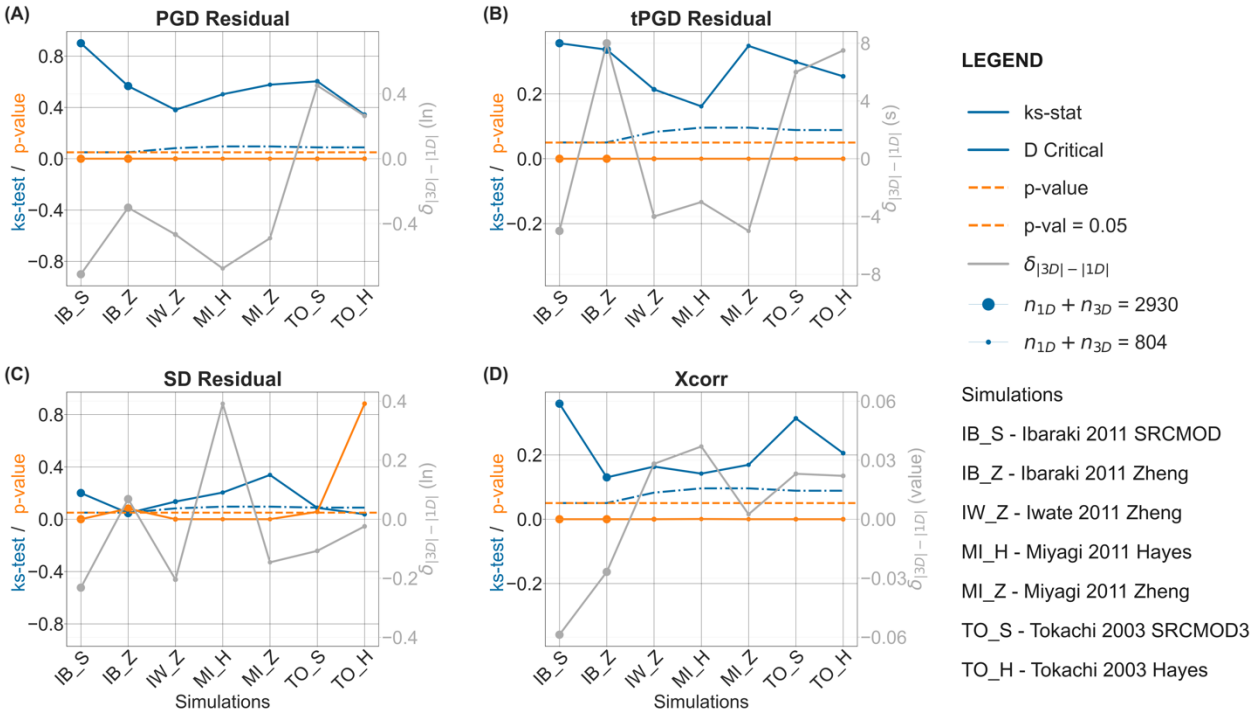

Fig. 11: KS-test results and median residual difference between entire MudPy 1D and SW4 3D residual distributions for all simulations. The points are sized by the population size in that bin. Blue solid lines represent the K-S statical (ks-stat) value, blue dash-dotted lines represent the critical value, orange solid lines represent the p value, orange dashed lines represent the p value line of 0.05, and the gray solid line represents the median residual difference of zero.

Effect of 3D structure in the upper 0-30 km

To understand if a well-constrained shallow structure plays a larger role than deeper structure in accurately modeling time-dependent crustal deformation from mid-crustal earthquakes, we tested the effect of 3D structure in the upper 0-30 km on our simulations using the Ibaraki 2011 and Miyagi 2011 earthquakes

as case studies. The Ibaraki 2011 earthquake is located at 43.2 km which is below the upper 0-30 km, while the Miyagi earthquake has a focal depth of 8.3 km, so the earthquake is within the 0-30 km structure (Fig. 1 and 12). We used the upper 0-30 km of the 3D structure because it is the depth region where we observed the most lateral structural heterogeneity.

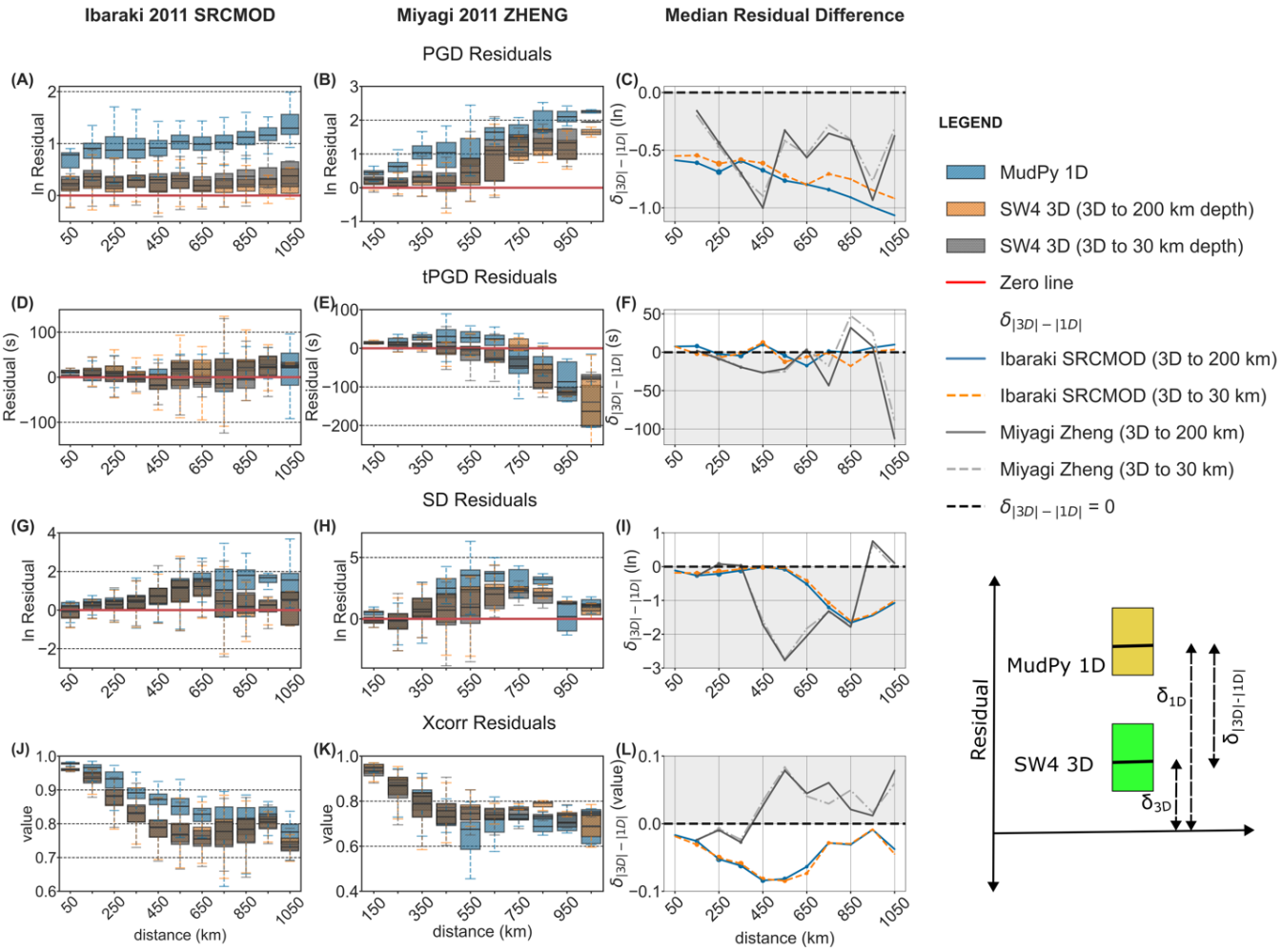

Fig. 12: Effect of 3D structure in the upper 0-30 km depth on PGD, t_{PGD}, SD residuals and cross correlation values for Ibaraki 2011 and Miyagi 2011A earthquakes. We compare the MudPy 1D and SW4 3D residuals using 200 km- and 30 km-3D structure at different hypocentral distances. Ibaraki 2011 earthquake is located at 43.2 km depth while Miyagi 2011A earthquake is located at 8.3 km depth, so it is located within the upper 0-30 km depth. The figures on the right column show the median residual difference for the PGD, t_{PGD}, SD residuals and cross correlation values for two simulations compared to the MudPy residuals. Blue boxplots (slant lines hatched style): MudPy 1D residuals; orange boxplots (diamond hatch style): SW4 3D simulation using 200 km-3D structure; gray boxplots (circle hatched style); SW4 3D simulation with 3D structure up to 30 km depth; red horizontal line: zero residual line; blue solid lines: median residual difference for the simulation using the 200 km-3D structure; orange solid line: median residual difference for the 30-km-3D structure; gray shaded regions in left column: regions where "3D fits better than 1D"; white regions represent "1D fits better than 3D". Bottom right schematic is a visual representation of the meaning of the residuals presented here.

To do this, we created another rfile for a 3D velocity model involving only the upper 0-30 km depth of the unified 3D velocity model of Japan, which is an extrapolated version of the 3D Japan Integrated Velocity Structure Model (Koketsu et al., 2008, 2009). The SW4 simulation is setup to use the 3D structure up to 30 km depth and a 1D velocity model, similar to the MudPy 1D simulations from 30 km to 200 km depth.

The residuals for the Ibaraki 2011 and Miyagi 2011 earthquake simulations involving 30km-depth 3D structure (3D_30km) and the 200km-depth 3D structures (3D_200km) are consistently lower than residuals from a purely 1D simulations without any 3D structure (Fig. 12). Comparing the two SW4 simulations to the MudPy 1D simulation reveals that the residual values from the 3D_30km simulation are similar to the residuals from the 3D_200km simulation up to a hypocentral distance of about 600 km. However, the residual using the 3D_200km simulation is smaller (i.e., better fit) than the 3D_30km simulation above the 600 km distance. The static displacement residuals are similar at all distances.

This result shows that the reduction of the PGD residuals in the 3D simulations is a combined effect of both shallow and deep 3D structures at hypocentral distances >~600 km. Hence, incorporating only the upper 30 km of a 3D structure will still improve the fit to the observed PGD values compared to purely 1D simulations, especially in regions where a deep 3D structure is not available. In other words, the 30km-depth structure plays a role in reducing the PGD residuals, but since the PGD residual compared to the observed waveforms is further reduced in the 3D_200km simulation for larger hypocentral distances, the deeper structure still contributes to the lower residuals. This result is important both in understanding what scale of structure should be included in 3D models, but also in estimating the computational demand in accurately modeling these time series.

Effect of maximum frequency on the waveform intensity measures

Another important question is whether the reduction in the residuals between observed and SW4 3D simulations will persists at higher maximum frequency. To answer the question, we generated 0.50 Hz synthetic waveforms for all the four earthquakes using SW4. We varied the lateral extent of the 3D domain geometry depending on location of each earthquake, thus fewer stations, (Fig. S5) and used one of the 100 ruptures from the FakeQuakes realizations of the mean rupture models to reduce computational cost (Supplementary material S3). We compared only the intensity measures from the common stations between the 1D and 3D simulations.

For the Ibaraki 2011 earthquakes, we observed similar trends in the PDG, t_{PGD}, SD residuals and cross correlation values compared to the 0.25 Hz SW4 3D simulation (Fig. 13). However, the median residual difference in the PGD residual compared to the MudPy 1D simulation shows a consistent further reduction in the 0.5 Hz simulation. Hence, even though the overall trend in the residuals persists between the 0.25 Hz and 0.50 Hz simulations, the 0.50 Hz better fits the observed waveforms. Figure 14 shows the PGD residuals for the other earthquakes and rupture models. The figure further validates the reduction in the residual in the 0.50 Hz simulations, except for the Tokachi earthquake (Fig. 14).

CONCLUSIONS AND FUTURE WORK

We present 1D and 3D simulations of four **M**7.3+ earthquakes in Japan and showed the need to include realistic 3D structure with modern computational approaches and avoid the oversimplification of 1D GNSS models. In the 1D simulations, using different rupture models, PGD residuals do not change significantly with distance for the same earthquake. Therefore, any deviations in the PGD residual for the same rupture model in 3D simulations reveal the effect of the 3D structure. Comparing 1D and 3D residuals, we observed that 3D simulations show improved fits to the observed waveforms, demonstrating that the unmodeled waveform in

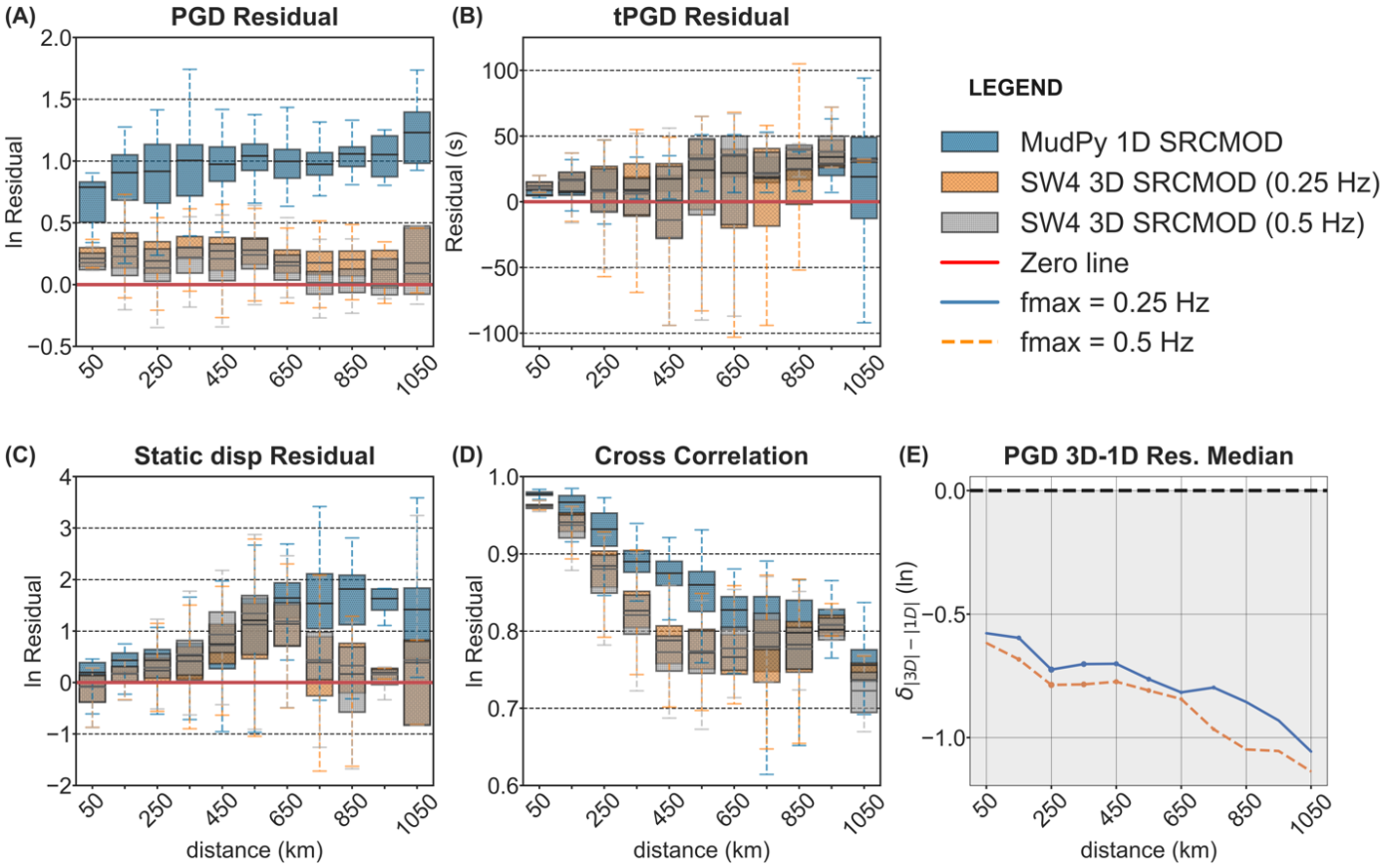

Fig. 13: Effect of the maximum frequency (fmax) on PGD, t_{PGD}, SD residuals and cross correlation values for Ibaraki 2011 earthquake (using rupture 5 with SRCMOD mean rupture model). Blue boxplots (circle hatched style): MudPy 1D residuals; orange boxplots (diamond hatch style): SW4 3D simulation with fmax of 0.25 Hz; gray boxplots (crossed hatched style): SW4 3D simulation with fmax of 0.50 Hz; red horizontal line: zero residual line. Figure (E) shows the median residual difference for the PGD residuals compared to the MudPy residuals. Blue solid and orange dash lines represent the median residual difference for the simulation with fmax of 0.25 Hz and 0.50 Hz, respectively.

the 1D simulation is due to the structure (path). However, the observed overall trends in 1D and 3D residuals with distance are likely related to a source model derived with the assumption of 1D structure or the variation of attenuation parameters within each layer in the 3D structure.

PGD median residuals with distance show that 3D simulations consistently have lower residuals for all simulations, except for Tokachi 2003. The t_{PGD} median residuals are consistently closer to zero for the 3D simulations, generally between 250 km and 700 km distance and up to 1150 km for Iwate 2011 earthquake. The SD median residuals are similar in both 1D and 3D simulations up to about 400 or 500 km, but the 3D

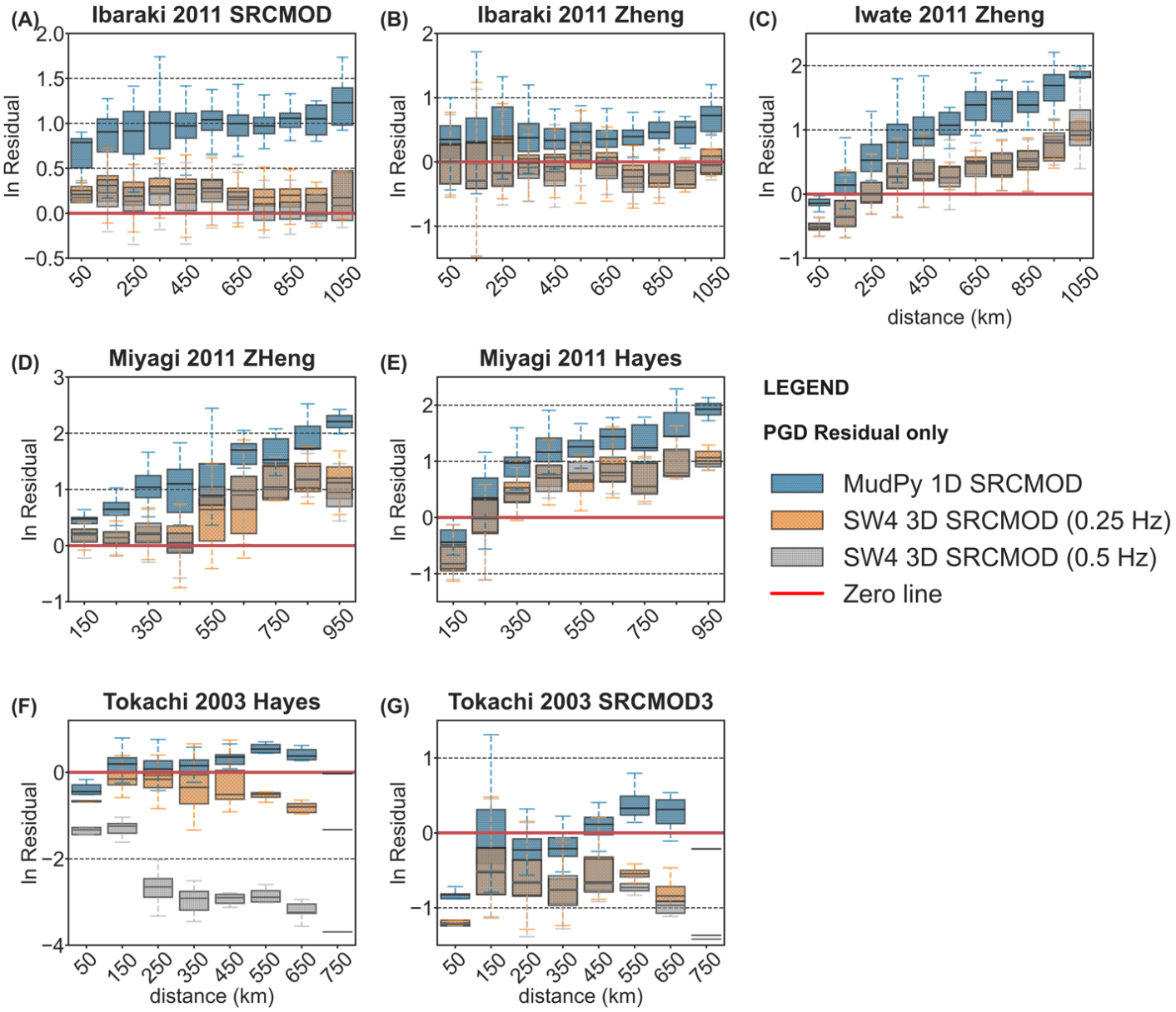

Fig. 14: Effect of the maximum frequency (fmax) on PGD for all the simulations. The blue boxplots (circle hatched style) represent the MudPy 1D residuals. The orange boxplots (diamond hatch style) represent the SW4 3D simulation with fmax of 0.25 Hz. The gray boxplots (crossed hatched style) represent the SW4 3D simulation with fmax of 0.50 Hz. The red horizontal line represents the zero residual line.

simulations fit better at greater distances. The cross-correlation median values are slightly higher in the 3D simulation above hypocentral distance of about 300 km, except for the Ibaraki 2011 earthquake. The KS tests show that the distributions of the PDG residuals in the 1D and 3D simulations are significantly different for all simulations up to 1000 km distance and 800 km for the Iwate 2011 earthquake. The intensity measures for

each simulation without considering the variation with distance also show a general reduction in values in the 3D simulations compared to 1D simulations.

This study also shows that the reduction of the PGD residuals in the 3D simulations is a combined effect of both shallow and deep 3D structures especially above certain hypocentral distances. Incorporating only the upper 30 km 3D structure will still improve the fit to the observed PGD values. Lastly, depending on the level of desired model accuracy and available computational resources, the 0.25 Hz SW4 3D simulations may be sufficient to model the kinematics and time-dependent crustal deformation measured by GNSS. Our results demonstrate that future studies of time-dependent crustal deformation should consider using 3D structure or Green's functions, in particular when peak intensity measures such as PGD are the most critical.

Data and Resources

SW4 is an open-source code and available at https://github.com/geodynamics/sw4 (last accessed January 2023) hosted by the Computational Infrastructure for Geodynamics ((http://geodynamics.org). MudPy and FakeQuakes are available at https://github.com/oluwaseunfadugba/MudPy. Our maps were made with PyGMT (Uieda et al., 2022) available at https://github.com/GenericMappingTools/pygmt. PyGMT wraps around GMT6 (Wessel et al., 2019). We used the Slab2.0 model (Hayes, 2018) to create a fault geometry mesh for the Japan Trench using Gmsh (Geuzaine and Remacle, 2009). Our figures were made with Python 3 (Van Rossum & Drake, 2009), Seaborn (Waskom, 2021), Pandas (McKinney et al., 2010), and ObsPy (Beyreuther, et al., 2010). Our codes are available at https://github.com/oluwaseunfadugba/1D_vs_3D_HR-GNSS_CrustalDeformation. The GNSS stations, mesh, 3D velocity model, projected rupture models for each earthquake on the Japan Trench mesh, the codes at the time of publication and the corresponding 100 realizations of the mean rupture models generated using FakeQuakes are available on Zenodo (https://doi.org/10.5281/zenodo.7765170).

Acknowledgements

This work was funded by NASA ROSES grant 80NSSC21K0841. SW4 simulations were performed on the Lassen graphics processing unit accelerated platform operated by Livermore Computing using a Computing Grand Challenge allocation and on Talapas High Performance Computing at the University of Oregon. This work was performed in part under the auspices of the U.S. Department of Energy by Lawrence Livermore National Laboratory under Contract DE-AC52-07NA27344. We thank the Computational Infrastructure for Geodynamics (http://geodynamics.org) which is funded by the National Science Foundation under awards EAR-0949446 and EAR-1550901.

Author contributions

Conceptualization: O.F., V.S., D.M.. Data Curation: O.F., V.S., D.M., R.S.. Formal Analysis: O.F, V.J., D.M.. Funding Acquisition: V.S., D.M.. Investigation: All authors. Methodology: All authors. Project Administration: O.F, V.S., D.M.. Resources: O.F., V.J., D.M., A.R.. Software: D.M., A.R.. Supervision: V.S, D.M., A.R.. Validation: O.F., V.S., D.M.. Visualization: O.F., V.S., D.M.. Writing – original draft: O.F, V.S., D.M.. Writing – review & editing: All authors.

REFERENCES

Aagaard, B. T., Knepley, M. G., and Williams, C. A. (2013), A domain decomposition approach to implementing fault slip in finite-element models of quasi-static and dynamic crustal deformation, Journal of Geophysical Research: Solid Earth, 118, 3059– 3079, doi:10.1002/jgrb.50217.

Baltay A.S., T. C. Hanks, and N. A. Abrahamson (2017). Uncertainty, Variability, and Earthquake Physics in Ground-Motion Prediction Equations. Bulletin of the Seismological Society of America, Vol. 107, No. 4, pp. 1754–1772, August 2017, doi: 10.1785/0120160164.

Beyreuther, M., Barsch, R., Krischer, L., Megies, T., Behr, Y., and Wassermann, J. (May/June 2010). ObsPy: A Python Toolbox for Seismology, Seismological Research Letters, 81 (3), 530-533. http://www.seismosoc.org/publications/SRL/SRL_81/srl_81-3_es/

Bock, Y., Melgar, D., Crowell, B.W. (2011). Real-Time Strong-Motion Broadband Displacements from Collocated GPS and Accelerometers. Bulletin of the Seismological Society of America (2011) 101 (6): 2904–2925, doi: 10.1785/0120110007.

Delouis, B., Nocquet, J. M., & Vallée, M. (2010). Slip distribution of the February 27, 2010 Mw= 8.8 Maule earthquake, central Chile, from static and high-rate GPS, InSAR, and broadband teleseismic data. Geophysical Research Letters, 37(17).

Dziewonski, A. M., & Anderson, D. L. (1981). Preliminary reference Earth model. Physics of the earth and planetary interiors, 25(4), 297-356.

Furumura, T., and B. L. N. Kennett (1998). On the nature of regional seismic phases-III. The influence of crustal heterogeneity on the wavefield for subduction earthquakes: The 1985 Michoacan and 1995 Copala, Guerrero, Mexico earthquakes, Geophys. J. Int. 135, no. 3, 1060–1084.

Furumura, T., and S. K. Singh (2002). Regional wave propagation from Mexican subduction zone earthquakes: The attenuation functions for interplate and inslab earthquakes, Bull. Seismol. Soc. Am. 92, no. 6, 2110–2125.

Furumura, T., & Kennett, B. L. N. (2005). Subduction zone guided waves and the heterogeneity structure of the subducted plate: Intensity anomalies in northern Japan. Journal of Geophysical Research: Solid Earth, 110(B10).

Goldberg, D. E., Koch, P., Melgar, D., Riquelme, S., & Yeck, W. L. (2022). Beyond the Teleseism: Introducing Regional Seismic and Geodetic Data into Routine USGS Finite-Fault Modeling. Bulletin of the Seismological Society of America, 93(6), 3308-3323. https://doi.org/10.1785/0220220047

Goldberg, D. E., & Melgar, D. (2020). Generation and validation of broadband synthetic P waves in semistochastic models of large earthquakes. Bulletin of the Seismological Society of America, 110(4), 1982-1995.

Geng, J., Pan, Y., Li, X., Guo, J., Liu, J., Chen, X., & Zhang, Y. (2018). Noise characteristics of high-rate multi-GNSS for subdaily crustal deformation monitoring. Journal of Geophysical Research: Solid Earth, 123(2), 1987-2002.

Geuzaine, C. and Remacle, J.-F. (2009), Gmsh: A 3-D finite element mesh generator with built-in pre- and post-processing facilities. International Journal for Numerical Methods in Engineering, 79: 1309-1331. https://doi.org/10.1002/nme.2579.

Graves, R. (2014). Standard Rupture Format Version 2.0.

Hayes, G. (2018). Slab2 - A Comprehensive Subduction Zone Geometry Model [Data set]. U.S. Geological Survey. https://doi.org/10.5066/F7PV6JNV

Hearn E.H. & R. Burgmann (2005). The Effect of Elastic Layering on Inversions of GPS Data for Coseismic Slip and Resulting Stress Changes: Strike-Slip Earthquakes. Bulletin of the Seismological Society of America, Vol. 95, No. 5, pp. 1637–1653, October 2005, doi: 10.1785/0120040158

Hill, E.M., Borrero, J.C., Huang, Z., Qiu, Q., Banerjee, P., Natawidjaja, D.H., Elosegui, P., Fritz, H.M., Suwargadi, B.W., Pranantyo, I.R. and Li, L., 2012. The 2010 Mw 7.8 Mentawai earthquake: Very shallow source of a rare tsunami earthquake determined from tsunami field survey and near-field GPS data. Journal of Geophysical Research: Solid Earth, 117(B6).

Ide, S. (2007). Slip Inversion. Earthquake seismology 4, 193-223, doi: 10.1016/B978-044452748-6.00068-7.

Kanamori, H. (1972). Mechanism of tsunami earthquakes. Physics of the earth and planetary interiors, 6(5), 346-359.

Koketsu, K., Hikima, K., Miyazaki, S. I., & Ide, S. (2004). Joint inversion of strong motion and geodetic data for the source process of the 2003 Tokachi-Oki, Hokkaido, earthquake. Earth, Planets and space, 56, 329-334.

Koketsu, K., Miyake, H., Fujiwara, H. and Hashimoto, H. (2008). Progress towards a Japan integrated velocity structure model and long-period ground motion hazard map, Proceedings of the 14th World Conference on Earthquake Engineering, Paper No. S10-038.

Koketsu K., Miyake H. and Afnimar Tanaka Y. (2009). A proposal for a standard procedure of modeling 3-D velocity structures and its application to the Tokyo metropolitan area, Japan, Tectonophysics 472, 290–300.

Kolmogorov A (1933). "Sulla determinazione empirica di una legge di distribuzione". Giornale dell'Istituto Italiano degli Attuari, 4: 83–91. 5.

Kotha, S.R., G. Weatherill, D. Bindi, F. Cotton (2020). A regionally-adaptable ground-motion model for shallow crustal earthquakes in Europe. Bulletin of Earthquake Engineering (2020) 18:4091–4125 https://doi.org/10.1007/s10518-020-00869-1.

Kubo, H., Asano, K., and Iwata, T. (2013), Source-rupture process of the 2011 Ibaraki-Oki, Japan, earthquake (Mw 7.9) estimated from the joint inversion of strong-motion and GPS Data: Relationship with seamount and Philippine Sea Plate, Geophysical Research Letters, 40, 3003–3007, doi:10.1002/grl.50558.

Kuehn, N.M. and NA Abrahamson (2020). Spatial correlations of ground motion for non-ergodic seismic hazard analysis. Earthquake Engineering Structure Dynamics, 49:4-23. https://doi.org/10.1002/eqe.3221.

Landwehr N., N. M. Kuehn, T. Scheffer, and N. Abrahamson (2016). A Nonergodic Ground-Motion Model for California with Spatially Varying Coefficients. Bulletin of the Seismological Society of America, Vol. 106, No. 6, pp. 2574–2583, December 2016, doi: 10.1785/0120160118

Langer, L., Gharti, H.M. and J. Tromp (2019). Impact of topography and three-dimensional heterogeneity on coseismic deformation, Geophysical Journal International, Volume 217, Issue 2, May 2019, Pages 866–878, https://doi.org/10.1093/gji/ggz060.

Langer, L., Beller, S., Hirakawa, E. and J. Tromp (2023). Impact of sedimentary basins on Green's functions for static slip inversion, Geophysical Journal International, Volume 232, Issue 1, January 2023, Pages 569–580, https://doi.org/10.1093/gji/ggac344

Laske, G., Masters, G., Ma, Z., & Pasyanos, M. (2013, April). Update on CRUST1. 0—A 1-degree global model of Earth's crust. In Geophysical research abstracts (Vol. 15, No. 15, p. 2658). Vienna, Austria: EGU General Assembly.

Maeda, T., S. Takemura, and T. Furumura (2017), OpenSWPC: An open-source integrated parallel simulation code for modeling seismic wave propagation in 3D heterogeneous viscoelastic media, Earth Planets Space, 69, 102. doi:10.1186/s40623-017-0687-2

Mann, M. E., & Abers, G. A. (2020). First-order mantle subduction-zone structure effects on ground motion: The 2016 Mw 7.1 Iniskin and 2018 Mw 7.1 Anchorage earthquakes. *Seismological Research Letters*, *91*(1), 85-93.

McKinney, W., & others. (2010). Data structures for statistical computing in python. In Proceedings of the 9th Python in Science Conference (Vol. 445, pp. 51–56).

Melgar, D., Crowell, B. W., Melbourne, T. I., Szeliga, W., Santillan, M., & Scrivner, C. (2020). Noise characteristics of operational real-time high-rate GNSS positions in a large aperture network. Journal of Geophysical Research: Solid Earth, 125(7), e2019JB019197.

Melgar, D., LeVeque, R. J., Dreger, D. S., & Allen, R. M. (2016). Kinematic rupture scenarios and synthetic displacement data: An example application to the Cascadia subduction zone. Journal of Geophysical Research: Solid Earth, 121(9), 6658-6674.

Melgar, D., Ganas, A., Taymaz, T., Valkaniotis, S., Crowell, B. W., Kapetanidis, V., Tsironi, V., Yolsal-Çevikbilen, S., & Öcalan, T. (2020). Rupture kinematics of 2020 January 24 M w 6.7 Doğanyol-Sivrice, Turkey earthquake on the East Anatolian Fault Zone imaged by space geodesy. Geophysical Journal International, 223(2), 862-874.

Melgar, D., & Bock, Y. (2015a). Kinematic earthquake source inversion and tsunami runup prediction with regional geophysical data. Journal of Geophysical Research: Solid Earth, 120(5), 3324-3349.

NOAA National Geophysical Data Center (2009) ETOPO1 1 Arc-Minute Global Relief Model. NOAA National Centers for Environmental Information. Accessed [10/14/2021].

Ozawa, S., Nishimura, T., Suito, H., Kobayashi, T., Tobita, M. & Imakiire, T. (2011). Coseismic and postseismic slip of the 2011 magnitude-9 Tohoku-Oki earthquake. Nature, 475(7356), 373-376. doi: 10.1038/nature10227

Petersson, N.A.; Sjögreen, B. (2012), Stable and efficient modeling of anelastic attenuation in seismic wave propagation, Communications in Computational Physics, 12 (01), 193-225

Petersson, N.A.; Sjögreen, B. (2015), Wave propagation in anisotropic elastic materials and curvilinear coordinates using a summation-by-parts finite difference method, Journal of Computational Physics, 299, 820-841, doi: 10.1016/j.jcp.2015.07.023.

Petersson, N.A.; Sjögreen, B. (2017), User's guide to SW4, version 2.0, LLNL-SM-741439 (LLNL-SM-741439)

Petersson, N.A.; Sjögreen, B. (2017), SW4, version 2.01 [software], Computational Infrastructure of Geodynamics, doi: 10.5281/zenodo.1063644.

Rodgers, A. J., A. Pitarka, R. Pankajakshan, B. Sjögreen, and N. A. Petersson (2020). Regional-Scale 3D Ground-Motion Simulations of Mw 7 Earthquakes on the Hayward Fault, Northern California Resolving Frequencies 0–10 Hz and Including Site-Response Corrections, Bull. Seismol. Soc. Am. 110, 2862–2881, doi: 10.1785/0120200147

Ruhl, C. J., D. Melgar, J. Geng, D. E. Goldberg, B. W. Crowell, R. M. Allen, Y. Bock, S. Barrientos, S. Riquelme, J. C. Baez, et al. (2019). A global database of strong-motion displacement GNSS recordings and an example application to PGD scaling. Seismological Research Letters, 90(1), 271-279.

Sahakian, V. J., Melgar, D., Quintanar, L., Ramírez-Guzmán, L., Pérez-Campos, X., & Baltay, A. (2018). Ground motions from the 7 and 19 September 2017 Tehuantepec and Puebla-Morelos, Mexico, earthquakes. *Bulletin of the Seismological Society of America*, *108*(6), 3300-3312.

Sahakian, V. J., Baltay, A., Hanks, T. C., Buehler, J., Vernon, F. L., Kilb, D., & Abrahamson, N. A. (2019). Ground motion residuals, path effects, and crustal properties: A pilot study in Southern California. *Journal of Geophysical Research: Solid Earth*, *124*(6), 5738-5753.

Sahakian V.J., Melgar D., and M. Muzli (2019b). Weak Near-Field Behavior of a Tsunami Earthquake. Geophysical Research Letters. 46:9519–9528. doi:10/1029/2019GL083989

Smirnov N (1948). "Table for estimating the goodness of fit of empirical distributions". Annals of Mathematical Statistics. 19 (2): 279–281. doi:10.1214/aoms/1177730256.

Sjögreen, B.; Petersson, N.A. (2012), A Fourth Order Accurate Finite Difference Scheme for the Elastic Wave Equation in Second Order Formulation, Journal of Scientific Computing, 52 (1) , 17-48, doi: 10.1007/s10915-011-9531-1.

Tung, S., & Masterlark, T. (2018). Sensitivities of near-field tsunami forecasts to megathrust deformation predictions. Journal of Geophysical Research: Solid Earth, 123(2), 1711-1735.

Uieda, L., Tian, D., Leong, W. J., Toney, L., Schlitzer, W., Yao, J., Grund, M., Jones, M., Materna, K., Newton, T., Ziebarth, M., and P., Wessel (2021). PyGMT: A Python interface for the Generic Mapping Tools, version v0.3.1, Zenodo, https://doi.org/10.5281/zenodo.4592991.

Van Rossum, G., & Drake, F. L. (2009). Python 3 Reference Manual. Scotts Valley, CA: CreateSpace.

Wald, D. J., and Graves, R. W. (2001), Resolution analysis of finite fault source inversion using one- and three-dimensional Green's functions: 2. Combining seismic and geodetic data, Journal of Geophysical Research, 106(B5), 8767– 8788, doi:10.1029/2000JB900435.

Wallace, L. M., Kaneko, Y., Hreinsdóttir, S., Hamling, I., Peng, Z., Bartlow, N., ... & Fry, B. (2017). Large-scale dynamic triggering of shallow slow slip enhanced by overlying sedimentary wedge. *Nature Geoscience*, *10*(10), 765-770.

Waskom, M. L. (2021). Seaborn: statistical data visualization, Journal of Open Source Software, 6 (60), pp 3021. https://doi.org/10.21105/joss.03021.

Wessel, P., Luis, J. F., Uieda, L., Scharroo, R., Wobbe, F., Smith, W. H. F., & Tian, D. (2019). The Generic Mapping Tools version 6. Geochemistry, Geophysics, Geosystems, 20, 5556–5564. https://doi.org/10.1029/2019GC008515

Williams, C. A., and L. M. Wallace (2015), Effects of material property variations on slip estimates for subduction interface slow-slip events, Geophysical Research Letters, 42, 1113–1121, doi:10.1002/ 2014GL062505.

Wirth, E. A., Sahakian, V. J., Wallace, L. M., & Melnick, D. (2022). The occurrence and hazards of great subduction zone earthquakes. *Nature Reviews Earth & Environment*, *3*(2), 125-140.

Yamanaka, Y. & Kikuchi, M. (2003). Source process of the recurrent Tokachi-Oki earthquake on September 26, 2003, inferred from teleseismic body waves. Earth, Planets and Space, 55(12), e21–e24.

Yagi, Y. (2004). Source rupture process of the 2003 Tokachi-Oki earthquake determined by joint inversion of teleseismic body wave and strong ground motion data. Earth, Planets and space, 56, 311-316.

Yue, H., & Lay, T. (2011). Inversion of high-rate (1 sps) GPS data for rupture process of the 11 March 2011 Tohoku earthquake (Mw 9.1). Geophysical Research Letters, 38(7).

Zhang, H., Melgar, D., Sahakian, V., Searcy, J., & Lin, J. T. (2022). Learning source, path and site effects: CNN-based on-site intensity prediction for earthquake early warning. *Geophysical Journal International*, *231*(3), 2186-2204.

Zheng, X., Y. Zhang, R. Wang, L. Zhao, W. Li, and Q. Huang (2020). Automatic inversions of strong-motion records for finite-fault models of significant earthquakes in and around Japan, Journal Geophysical Research 125, no. 9, e2020JB019992, doi: 10.1029/ 2020JB019992.